PHOTONICS Research

Observation of maximal intrinsic chirality empowered by dual quasi-bound states in the continuum in a planar metasurface

Xin Qi,[1,†] Jiaju Wu,[1,†] Feng Wu,[2] Song Zhao,[3] Chao Wu,[3,4] Yueyang Min,[1] Mina Ren,[1] Yufei Wang,[5,6] Haitao Jiang,[1] Yunhui Li,[1,4] Zhiwei Guo,[1] Yaping Yang,[1] Wanhua Zheng,[5] Hong Chen,[1] and Yong Sun[1,7]

[1]MOE Key Laboratory of Advanced Micro-Structured Materials, School of Physics Science and Engineering, Tongji University, Shanghai 200092, China
[2]School of Optoelectronic Engineering, Guangdong Polytechnic Normal University, Guangzhou 510665, China
[3]Shanghai Key Laboratory of Special Artificial Microstructure Materials and Technology, School of Physics Science and Engineering, Tongji University, Shanghai 200092, China
[4]Department of Electrical Engineering, Tongji University, Shanghai 201804, China
[5]State Key Laboratory on Integrated Optoelectronics, Institute of Semiconductors, Chinese Academy of Sciences, Beijing 100083, China
[6]e-mail: yufeiwang@semi.ac.cn
[7]e-mail: yongsun@tongji.edu.cn
[†]These authors contributed equally to this work.

Received 9 October 2023; revised 3 December 2023; accepted 4 December 2023; posted 4 December 2023 (Doc. ID 507081); published 29 January 2024

Metasurfaces with spin-selective transmission play an increasingly critical role in realizing optical chiral responses, especially for strong intrinsic chirality, which is limited to complex three-dimensional geometry. In this paper, we propose a planar metasurface capable of generating maximal intrinsic chirality and achieving dual-band spin-selective transmission utilizing dual quasi-bound states in the continuum (quasi-BICs) caused by the structural symmetry breaking. Interestingly, the value of circular dichroism (CD) and the transmittance of two kinds of circular polarization states can be arbitrarily controlled by tuning the asymmetry parameter. Remarkable CD approaching unity with the maximum transmittance up to 0.95 is experimentally achieved in the dual band. Furthermore, assisted by chiral BICs, the application in polarization multiplexed near-field image display is also exhibited. Our work provides a new avenue to flexibly control intrinsic chirality in planar structure and offers an alternative strategy to develop chiral sensing, multiband spin-selective transmission, and high-performance circularly polarized wave detection. The basic principle and design method of our experiments in the microwave regime can be extended to other bands, such as the terahertz and infrared wavelengths.

https://doi.org/10.1364/PRJ.507081

1. INTRODUCTION

Chirality is a widespread phenomenon in nature, defined as the inability to be superimposed with their own mirror image via either translation or rotation transformation [1], which is fundamental to many applications such as circular dichroism (CD) spectroscopy [2], information processing [3], biosensing [4,5], imaging [6–8], and broadband wave plate [9]. In nature materials, contribution from chiroptical effects on light–matter interaction is limited to the insignificant chirality of materials. Therefore, it is strongly desirable to achieve giant chiral responses with engineered structures [10]. Recently, chiral metasurfaces and metamaterials [11] with properly designed resonance units have been proposed, including folded metasurfaces [12], chiral mirrors [13,14], curled metasurfaces [15], multilayered structures [16], origami-based reconfigurable metamaterials [17], and fishnet structures [10,18], which show a broad prospect of application based on strong chiral responses. However, these intrinsically chiral materials are confined to complicated 3D structures [19–27], which lead to evident fabrication challenges. As a remedy, we can resort to the so-called extrinsic chirality of planar structures under oblique incidence [28,29]. However, planar structures with strong intrinsic chirality are preferrable for its irreplaceable ability to work efficiently under normal incidence [30] rather than oblique incidence.

Recently, a kind of special eigenmode of wave systems called bound states in the continuum (BICs) has offered an effective way to confine waves above the light cones embedded in the radiation continuum [31–34], which has been exploited in

applications such as sensors [35,36], lasers [37–39], nonlinear optics [40–42], near-field imaging [43], beam control [44–46], on-chip channel-less transmission [46,47], unidirectional radiation [48,49], and wireless power transfer [50]. In theory, BICs have vanishing linewidths and thus cannot be observed in the spectrum. In practice, through adding some perturbation, e.g., the symmetry breaking, the unobservable BIC evolves to a sharp Fano resonance, so-called quasi-BIC with ultrahigh Q-factor, that can be accessed externally [51–54]. Owing to the ultrahigh Q-factors, quasi-BICs can significantly enhance light–matter interaction, and hence provide a promising approach to boost chirality responses [28,55–64]. For example, K. H. Kim and J. R. Kim theoretically proposed a chiral dielectric metasurface that possesses giant chirality empowered by single quasi-BIC through breaking the in-plane inversion and mirror symmetries simultaneously [59]. Shi *et al.* revealed an exquisite planar design supporting one chiral quasi-BIC and observed experimentally near-perfect circular dichroism [60]. However, the intrinsic chirality of these metasurfaces empowered by quasi-BIC is restricted to a single chiral resonance. More importantly, the CD value cannot be controlled by adjusting structural parameters without frequency shifts. It limits the potential applications of chiral BIC on multiband spin selection. Therefore, achieving giant and tunable intrinsic chirality at multiple fixed wavelengths in a planar metasurface is still challenging yet desirable for polarization multiplexed applications.

In this paper, we theoretically and experimentally demonstrate a planar metasurface capable of generating maximal intrinsic chirality and achieving tunable dual-band spin-selective transmission through dual quasi-BICs. The gigantic intrinsic chirality and spin-selective transmission originate from the combined manipulation of the quasi-BICs and symmetry of the structure. By breaking either in-plane inversion symmetry or out-of-plane symmetry, the dual BICs can be transformed into dual quasi-BICs, and the chiral dual quasi-BICs can be constructed by breaking both symmetries simultaneously. Most importantly, the value of CD and the transmittance of two spin states [left circularly polarized (LCP) and right circularly polarized (RCP)] at dual band can be arbitrarily controlled by tuning the asymmetry parameter. Based on dual quasi-BICs, both the maximal transmittances are more than 0.94 of the chosen circularly polarized light, while its counterpart is close to zero. The measured maximal CD at two different frequencies approaches 0.95, with the maximum transmittance exceeding 0.9. Finally, as a potential application of the giant chiral response, the spin-dependent near-field image display based on the visualization of the metasurface consisting of chiral enantiomers is also exhibited. Our work provides a path to design chiral nonlinear optics devices [65], narrowband spin-selective pass filters [66], and circular polarization multiplexed sensors [67].

2. MODEL AND METHOD

An original schematic of the proposed planar metasurface is shown in Fig. 1(a). The unit cell possesses the C_3 rotational symmetry with period P, as shown in the inset. The original metasurface consists of an array of three parallel metal dimers

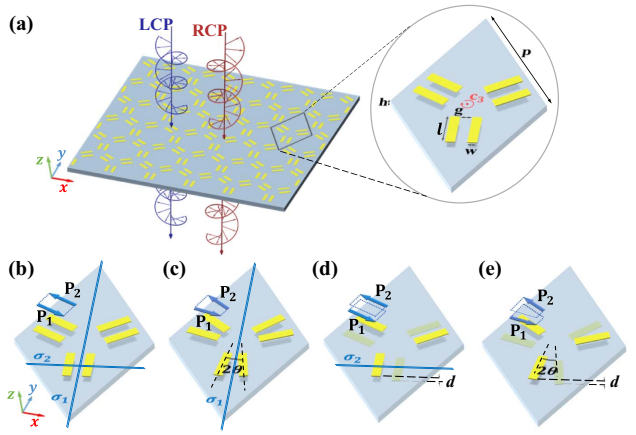

Fig. 1. (a) Schematic diagram of the original achiral metasurface supporting perfect BICs and a partial magnification of the lattice is shown on the right side. The unit cell with honeycomb lattice constant p consists of three dimers possessing the C_3 rotational symmetry. w and l are the width and length of each metal line in a dimer, respectively, and the gap between parallel metal wires is set to g. (b) Parallel metal wires and their lattice hosting dual BIC resonances. Two types of mirror symmetry planes, σ_1 and σ_2, satisfied by the dimer are indicated. (c), (d) Metal wires rotated by θ or vertically offset by d, respectively, and the unit cell of their lattice hosting dual quasi-BIC resonances but still no chirality. (e) Metal wires rotated by θ and vertically offset by d, and the unit cell of their lattice hosting dual quasi-BIC resonances with chirality. All metal wires are identical and the colors indicate location on different sides of dielectric slab. Relative orientation and offset of electric dipole moments characterizing BIC and quasi-BIC eigenstates are shown on the top for each dimer type.

supported by a commercial printed substrate F4BM ($\varepsilon_r = 2.2$, $\tan\delta = 0.009$). Here, the material of metal dimers is selected to be copper. One can see that the proposed dimer composed of two metal strips satisfies three types of mirror planes: two mirror symmetry planes σ_1 and σ_2, the normals of which are in the x–y plane, as shown in Fig. 1(b); and one mirror symmetry plane σ_3, the normal of which is out of the x–y plane. It is obvious that the original single-layer metasurface is achiral since its mirror symmetries are not broken. Therefore, the structure cannot distinguish between light with different pseudospins, i.e., LCP or RCP lights. To achieve giant chirality and spin-selective transmission in the spectra, one can simultaneously introduce two parameters, rotating angle θ [i.e., the metal strips rotate in the x–y plane at an angle θ around their respective centers, as shown in Fig. 1(c)] and vertical offset d [i.e., shifting a metal strip around the z direction, as shown in Fig. 1(d)] to establish a chiral metasurface that breaks all mirror symmetries, as illustrated in Fig. 1(e). It is worth noting that rotational deformation occurs in the x–y plane, breaking the in-plane symmetry, and the mirror symmetry plane σ_2 disappears. The introduction of vertical offset refers to the deformation in the z direction, which is considered to break the out-of-plane symmetry, and the mirror symmetry planes σ_1 and σ_3 disappear.

The time dependence of waves propagating along the positive direction is assumed as $e^{-i\omega t}$. The wave-polarized complex unit vectors are expressed as

$$\mathbf{e}_{\pm} = \frac{\mathbf{e}_x \mp i\mathbf{e}_y}{\sqrt{2}}, \tag{1}$$

where $\mathbf{e}_-$ and $\mathbf{e}_+$ correspond to LCP and RCP, respectively. Typically, such reflection-transmission problems can be described by an S-matrix equation. The key optical parameters to characterize the chiral response of the system are values of CD and optical rotation (OR):

$$\mathrm{CD} = \frac{|t_R|^2 - |t_L|^2}{|t_R|^2 + |t_L|^2}, \qquad \mathrm{OR} = [\arg(t_R) - \arg(t_L)]/2, \tag{2}$$

where t_L and t_R are the transmission coefficients of LCP and RCP, respectively. In the following, the underlying physical mechanism of chirality and spin-selective transmission will be clearly explained by manipulating symmetry of the structure.

The electric resonance of parallel metal strips excited by a normally incident wave can be characterized by a pair of electric dipole moments $\mathbf{P}_{1,2}$, as shown in Fig. 1(b). For an incident wave polarized along the unit vector $\mathbf{e}$, with a wave vector $\mathbf{k}$ along the z axis, its coupling with the eigenstates could be estimated through integrating the current density [56,68]:

$$m_{\mathbf{e}} \propto \int_{V_1, V_2}^{0} \mathrm{d}\mathbf{r}[\mathbf{j}(\mathbf{r}) \cdot \mathbf{e}]e^{ikz} = -i\omega(\mathbf{P}_1 \cdot \mathbf{e}e^{ikz_1} + \mathbf{P}_2 \cdot \mathbf{e}e^{ikz_2}), \tag{3}$$

where $m_{\mathbf{e}}$ is the coefficient describing the coupling of circularly polarized waves and dipole eigenstate; $\mathbf{j}(\mathbf{r})$ represents the current density; $\mathbf{P}_{1,2}$ are the dipole moments located at the metal surfaces; V_1 and V_2 are the volumes of a pair of metal strips, respectively; the dipole moments $\mathbf{P}_{1,2}$ are parallel or antiparallel, i.e., $\mathbf{P}_1 = \pm\mathbf{P}_2$, $z_1 = z_2$. When $\mathbf{P}_1 = -\mathbf{P}_2$, Eq. (3) can be written as $m_{\mathbf{e}} \propto \sum_i \mathbf{P}_i \cdot \mathbf{e}e^{ikz} = (\mathbf{P}_1 \cdot \mathbf{e} + \mathbf{P}_2 \cdot \mathbf{e})e^{ikz} = 0$, indicating that this eigenstate completely decouples from the incident wave for all polarizations due to symmetry protection. Interestingly, the antisymmetric eigenstate corresponds to BICs. However, perfect BICs are quite unusual since they have vanishing spectral linewidths and thus cannot be observed in the spectrum.

Next, we convert BICs to quasi-BICs with sharp Fano-type line profiles by breaking in-plane or out-of-plane symmetry and further introduce chirality to realize spin-selective transmission. First, we break the in-plane symmetry by introducing a rotating angle θ, which eliminates the mirror plane σ_2, as shown in Fig. 1(c). As a result, the dipole moments $\mathbf{P}_{1,2}$ no longer cancel each other out. The coupling coefficient can be derived from Eq. (3) as $m_+ = m_- \propto i\sqrt{2}p \sin\theta$, which means the opposing circularly polarized states are coupled to the structure. Therefore, by breaking in-plane symmetry, the BICs transform into the quasi-BICs. It is noted that the structure cannot yet distinguish between the two circularly polarized waves (i.e., LCP and RCP waves) due to $m_+ = m_-$ [56].

In addition to breaking in-plane symmetry, we can also break the out-of-plane symmetry to obtain quasi-BICs by introducing a small vertical offset d between the two metal sheets in the z direction indicated in Fig. 1(d). The actual displacement between dipoles is approximately equal to the relative vertical shift d of the metal strips, i.e., $d = z_1 - z_2$. Thus, the corresponding coupling coefficients for circularly polarized waves are $m_+ = m_- \propto pe^{ikd} \sin(kd/2)$, which means the structure is also achiral as the mirror plane σ_1 remains.

To obtain chirality, one needs to break all mirror symmetry planes of the structure through introducing vertical offset d and rotation angle θ simultaneously, as illustrated in Fig. 1(e). The coupling coefficient for different circularly polarized waves can be estimated as

$$m_{\pm} \propto pe^{ikd} \sin(\theta \mp kd/2), \tag{4}$$

which explains the emergence of resonances with chirality. Only if all symmetry planes are eliminated, the system at normal incidence is chiral, i.e., $m_+ \neq m_- \neq 0$ [28,56]. Later, we will prove our theoretical analysis.

3. RESULTS AND DISCUSSIONS

To confirm the above theoretical analysis, we perform numerical simulation by using a finite-element frequency-domain solver as a part of the CST Microwave Studio. The Floquet ports are utilized in the z direction, while periodic boundary conditions are imposed in the x–y plane. The dimensions of metal strips are $w = 3.6$ mm, $l = 14$ mm, and thickness $t = 0.035$ mm. The period of the unit cell p is 50 mm and the gap g is set to 7.3 mm. By breaking the in-plane symmetry, we first simulate the transmittance of the achiral metasurface at $d = 0$ mm as the rotation angle θ varies from 0° to 12° [corresponding to Fig. 1(c)], as shown in Fig. 2(a). Then, we also give the simulated transmittance of the structure as d varies from 0 to 2 mm [corresponding to Fig. 1(d)], by adjusting the thickness of the dielectric layer to break the out-of-plane symmetry at $\theta = 0°$, as illustrated in Fig. 2(b). It is worth mentioning that the offset d is approximately equal to the thickness h of the dielectric layer because the thickness of the dielectric layer is much larger than that of the metal wires ($h \gg t$). One can see that no matter whether in-plane symmetry or out-of-plane symmetry is broken individually, the transmittance spectra exhibit asymmetric Fano line shapes for LCP or RCP wave incidences, as shown in Figs. 2(a) and 2(b). We fit the quasi-BICs with the classical Fano resonance (see Appendix A). As the

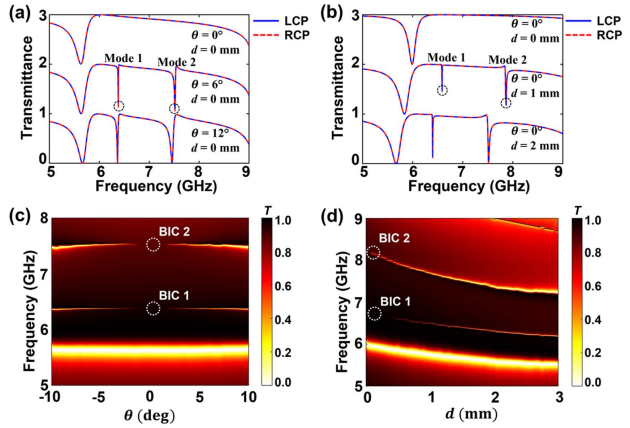

Fig. 2. Evolution of transmission spectra versus (a) divergence angle θ and (b) vertical d. (c), (d) Simulated transmission spectra of dual BICs by sweeping θ from −10° to 10° at $d = 0$ and d from 0 to 3 mm at $\theta = 0°$, respectively.

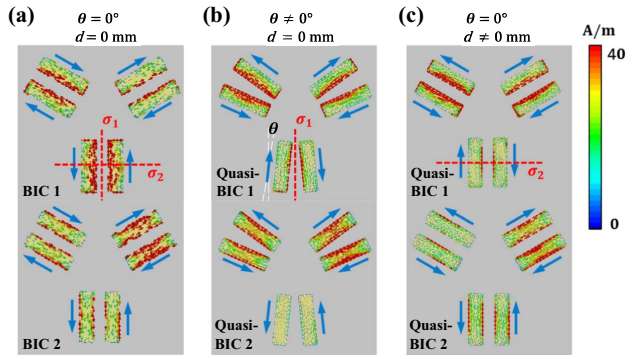

Fig. 3. (a) Surface current distribution of dual BICs. The unit cell possesses in-plane and out-of-plane mirror asymmetry. (b) Surface current distribution of dual quasi-BICs at $\theta = 0°$ and $d \neq 0$. (c) Surface current distribution of dual quasi-BICs at $d = 0$ and $\theta \neq 0°$.

symmetries of the structure are not completely broken, the transmittance spectra of the structure are identical for LCP and RCP waves.

Here, we are particularly interested in two branches of higher frequencies whose resonance linewidth enlarges noticeably as asymmetry parameters gradually increase. In particular, the resonance linewidth of the two modes disappears when external perturbation θ or d is zero since the antiparallel dipole moments are completely canceled. Namely, symmetry-protected dual BICs can be supported in the proposed structure where the two modes correspond to dual quasi-BICs [69–71]. Herein, we choose the LCP wave as a case to intuitively show the evolution of BICs to quasi-BICs and re-simulate the transmittance of the structure in a wider parameters range, as shown in Figs. 2(c) and 2(d). It can be clearly seen that symmetry-protected dual BICs appear when external perturbation θ and d are zero. Although the in-plane or out-of-plane symmetry of the structure can be broken by introducing asymmetry parameter θ or d, all mirror symmetry planes of the structure are not yet broken simultaneously. Therefore, the achiral structure results in identical electromagnetic response under the excitation of LCP and RCP waves.

As evidence for the quasi-BICs [corresponding to modes 1 and 2 in Fig. 2(a) or Fig. 2(b)] stems from symmetry-protected BICs, the surface current distribution and corresponding electric dipole moments for the LCP wave incidence with different asymmetry parameters are given in Fig. 3. The blue arrow indicates the electric dipole moments. Since the structure is achiral and the distribution of dipole moments for two distinct spin states is similar, here we only consider the case under the LCP wave incidence. One can see that each pair of electric dipoles at BICs frequencies is strictly antiparallel and cancels each other out when all mirror symmetry planes are preserved, as shown in Fig. 3(a). In other words, symmetry-protected dual BICs can exist in the structure. It should be pointed out that both BIC1 and BIC2 belong to symmetry-protected BICs but there are different eigenstates. As can be seen from Fig. 3(a), the surface currents are mainly concentrated on the inner side of the metal strips for BIC1, while they are concentrated on the two sides of the metal strips for BIC2. To transform perfect BICs into quasi-BICs, we first introduce an external perturbation, θ, to break the in-plane symmetry [52]. Dipole moments cannot completely cancel out because of the rotation angle $\theta \neq 0°$, as shown in Fig. 3(b). The corresponding coupling coefficient for different circularly polarized waves can be obtained from Eq. (3) as $m_e \propto \sum_i \mathbf{P}_i \cdot \mathbf{e} \neq 0$.

Another way to break symmetry is to introduce vertical offset d, which can break the out-of-plane symmetry [56,57]. When $\theta = 0°$, the surface currents are antiparallel but there exists an offset along the propagation direction of the incident wave so that the coupling coefficient between the localized state and the propagating wave is no longer zero, as shown in Fig. 3(c). Therefore, the leakage (coupling) of BICs to the propagating modes gives rise to the formation of quasi-BICs. Although there are minor differences in asymmetric Fano line shapes and surface currents under different ways of breaking symmetry, the dipole moments possess the same directions. Thus, the dual quasi-BICs resulting from arbitrary symmetry breaking are essentially identical, which is determined by the generation mechanism of the symmetry-protected BICs and the structure itself. However, no matter which way to break the symmetry, there will always be remaining mirror symmetry planes σ_1 or σ_2, as marked in Figs. 3(b) and 3(c), resulting in the structure being achiral, i.e., $m_+ = m_- \neq 0$.

Thus, to achieve the chiral responses, the offset d and rotation angle θ must be introduced simultaneously as indicated in Fig. 1(e), which means all mirror symmetry planes σ_1, σ_2, and σ_3 are broken. In this case, the metasurface is transparent to the incident wave of one spin state at the two frequencies where the quasi-BICs occur, while suppressing the transmission of its counterpart. We studied the dependence of the transmittance on divergence angle θ when offset $d = 2.2$ mm, as shown in Fig. 4(a). At $\theta = 0°$, the degeneracy of two spin states leads to an identical transmittance spectrum for both LCP and RCP waves. As the angle θ increases, the spin degeneracy is broken and an apparent asymmetry emerges in the transmission spectrum for different polarizations. It is obvious that the chirality and line shapes at dual quasi-BIC modes have changed dramatically. When $\theta = -8°$, the RCP incident wave is almost unobstructed at both quasi-BIC frequencies and maintains a high-efficiency transmittance over 0.92, while the transmittance of the LCP wave remarkably reduces to 0.05 (i.e., near zero). If we overturn d as −2.2 nm, the reversed spin-selective transmission at dual bands can be observed, as shown in Fig. 4(b). The reversed chirality can be explained as the inversion of coupling coefficients of eigenstates and different spin states, which can be quantified by Eq. (3).

We further studied how the chirality assisted by dual quasi-BICs changes with altering rotation angle. The CD spectra of the structure with $d = -2.2$ mm under varying θ indicate that the chiral response is also completely reversed when the divergence angle θ is rotated in the opposite direction, as shown in Fig. 4(c). At different structural parameter θ, the resonance frequencies basically do not shift while the CD values change. Specifically, the simulated CD of the lower-frequency branch grows steadily with increasing divergence angle θ up to the maximum (exceed ± 0.95) at $\theta = \pm 12°$ [blue line in Fig. 4(d)], while for the higher-frequency branch, the near-unity CD

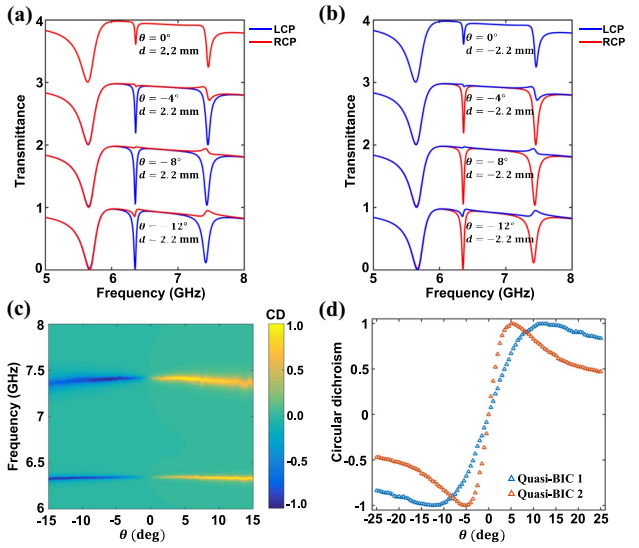

Fig. 4. Dependence of transmittance spectra of the structure on divergence angle θ at (a) $d = 2.2$ mm and (b) $d = -2.2$ mm. The blue and red lines represent LCP and RCP waves, respectively. (c) CD spectra of the structure with $d = -2.2$ mm versus rotated angles. (d) Circular dichroism with varying θ at dual quasi-BICs frequencies.

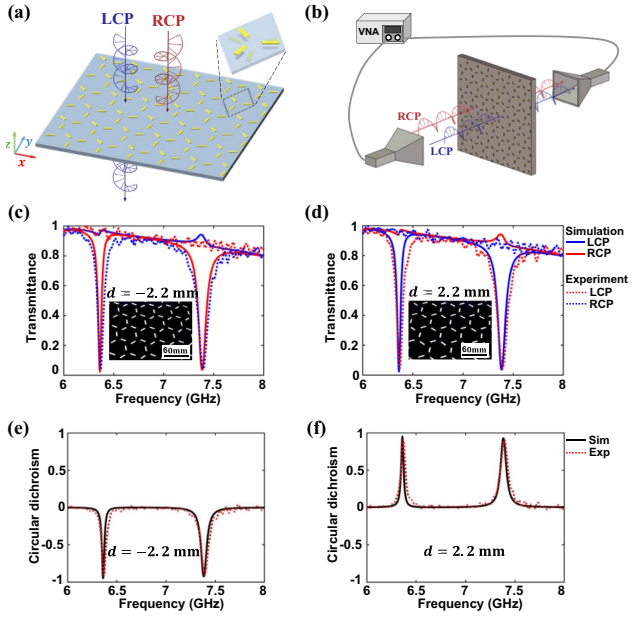

Fig. 5. (a) Schematic diagram of the original achiral metasurface supporting perfect BICs. (b) Schematic diagram of the microwave experimental setup. Measured (solid lines) and simulated (dashed lines) transmittance spectra of the normally incident co-polarized wave at (c) $d = -2.2$ mm and (d) $d = 2.2$ mm. The corresponding circular dichroism spectra at (e) $d = -2.2$ mm and (f) $d = 2.2$ mm.

occurs at $\theta = \pm 5°$ and the CD value reduced gradually as the divergence angle continued to increase [red line in Fig. 4(d)]. So far, we have demonstrated that the Fano line shapes and chirality of the multiband spin-selected resonances underpinned by dual quasi-BICs can be modified flexibly by simply tuning the divergence angle. It is worth mentioning that the intrinsic loss is also a necessary factor for maximum chirality (see Appendix B). Therefore, strong tunability makes it possible to realize dual maximum chiral quasi-BICs by using other materials or in other frequency regimes. As an example, we extend the chiral metasurface to terahertz (THz) wavelengths and prove that perfect dual-band circular dichroism can also be achieved (see Appendix C).

To experimentally demonstrate dual-band near-unity circular dichroism, copper and F4BM were selected as the metal and dielectric substrate, with thickness $t = 0.035$ mm and $h = 2.2$ mm, respectively. We set the structure parameters as $w = 3.6$ mm, $l = 9.4$ mm, and $\theta = 8°$ and etch copper strips on two sides of the dielectric substrate, as illustrated in Fig. 5(a). The sample is fabricated by standard printed-circuit-board technique on F4BM substrates. First, wet film printing and exposure are used to obtain development. Next, the pattern is electroplated and further etched to form a sample. The experimental measurements are performed in an anechoic chamber using microwave broadband horn antennas equipped with a vector-network analyzer (Agilent PNA network analyzer N5222A), as shown in Fig. 5(b). At $\theta = 8°$, the metasurface exhibits an almost perfect intrinsic chirality underpinned by BIC at 6.35 GHz and 7.43 GHz, as indicated in Fig. 4(d). The simulated and experimental transmission spectra of the metasurface with $d = \pm 2.2$ mm are plotted in Figs. 5(c) and 5(d), respectively. It can be observed that the multibands have giant chirality which is reversed when d is opposite. The theoretical and experimental CD spectra of the metasurface with the same thickness of dielectric plates but metal sheets distributed on opposite sides ($d = -2.2$ mm and $d = 2.2$ mm) are shown in Figs. 5(e) and 5(f), respectively. The CD value in simulation at two resonance frequencies can exceed 0.98 while that measured by experiment merely exceeds 0.95, which is mainly caused by the inaccurate loss of the sample material, whereas this small experimental error does not affect the basic results. It is worth noting that the CD spectra of RCP waves and LCP waves are reversed when the metal sheets are distributed on opposite sides. The result of the experiment is highly consistent with the theoretical simulations, verifying the existence of maximal intrinsic chiral resonances of the designed structure underpinned by BICs.

Finally, to exhibit the potential application in the multiband near-field image display of giant intrinsic chiral response empowered by dual quasi-BICs, we fabricated patterns containing numbers "0" or "1" using two enantiomers and simulated the electric field distribution under LCP and RCP incidence at different frequencies. The pattern array consists of approximately 16×8 cells [Fig. 6(a)], where different regions correspond to different enantiomers with the same θ but opposite $d = \pm 2.2$ mm, as shown in the insets. To achieve giant chirality in both bands, we choose $\theta = 8°$ where the simulated CD values of two modes exceed 0.9 and corresponding dual chiral BICs are at 6.35 GHz and 7.43 GHz denoted by patterns "0" and "1," respectively. Since the two enantiomers possess completely inverse chiral responses for circularly polarized waves, one can see that, under the LCP illumination, the electric field intensity distributions in the numbers "0" and "1" area are

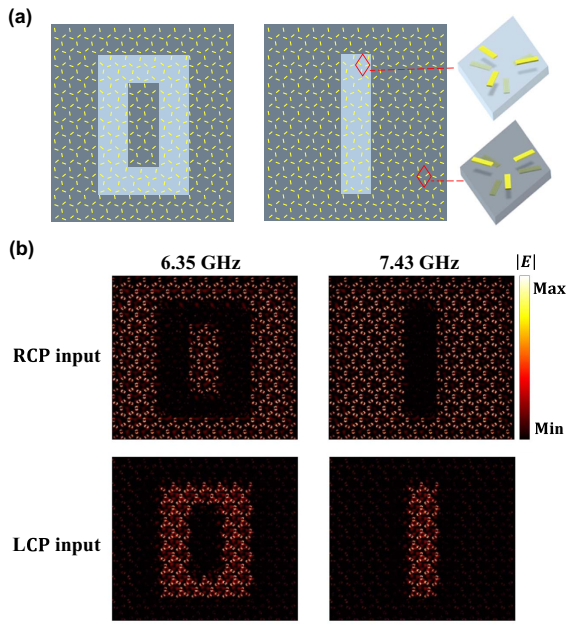

Fig. 6. (a) Construction of the pattern containing numbers "0" and "1." Insets show the partially magnified lattice. (b) Electric field intensity distributions (2 mm from the surface) of the proposed metasurface at 6.35 GHz and 7.43 GHz under the normal incidence of circularly polarized waves.

strong at two BICs frequencies due to resonant coupling with the LCP wave, while that in the remaining background area is weak because there is almost no resonance [the top row of Fig. 6(b)]. For the RCP incident wave, the opposite is true. The electric field in the area of the number is weak, while that in the background area is strong [the bottom row of Fig. 6(b)]. Therefore, the multiband near-field image display can be flexibly controlled by changing the polarization of the incident wave. And it is evident that the switch between "on" and "off" states for any BIC frequency can be independently realized by tuning divergence angle θ. It is worth pointing out that this near-field image display is formed through the highly localized electric field on the structural surface or inside [72,73], which is different from far-field holographic imaging [8]. The above results exhibit the potential application of chiral dual quasi-BICs in multifrequency polarization multiplexing near-field image display.

4. CONCLUSION

In summary, a chiral metasurface possessing maximal intrinsic chirality and dual-band spin-selective transmission underpinned by dual quasi-BICs is theoretically and experimentally investigated. By properly designing the asymmetric parameters, an almost perfect multiband circular dichroism (CD = 0.95) induced by dual quasi-BICs is observed experimentally, which is in good agreement with the numerical simulation, proving the validity of the proposed model. In addition, by changing the divergence angle θ, the line shapes and chirality of the dual-band resonances can be modified simultaneously. As a practical example, the polarization-multiplexed near-field image display assisted by dual quasi-BICs is also exhibited. Our work provides a new route to design multiband spin-selective resonators avoiding complicated 3D structures and oblique incidence. The designed planar metasurface supporting dual chiral quasi-BICs has great potential in applications such as spin-selective bio-detection, on-chip chiral manipulation, and chemical analysis.

APPENDIX A: FANO FITTING OF DUAL QUASI-BICS

Two asymmetric resonances originated from the interference between the dipole moment of metal wires and the continuum-free space. In Figs. 7(a) and 7(b), as $d = 0$ mm, we fit the curves of dual quasi-BICs when $\theta = 6°$ and $\theta = 12°$ with the classical Fano formula

$$T(\omega) = T_0 + A_0 \frac{[q + 2(\omega - \omega_0)/\tau]^2}{1 + [2(\omega - \omega_0)/\tau]^2}, \tag{A1}$$

where T_0 is the transmission, q denotes the Breit–Wigner–Fano parameter, A_0 represents the continuum-discrete coupling constant, ω_0 is the resonant frequency, and τ is the resonant linewidth. The Q of quasi-BICs can be evaluated with $Q = \omega_0/\tau$.

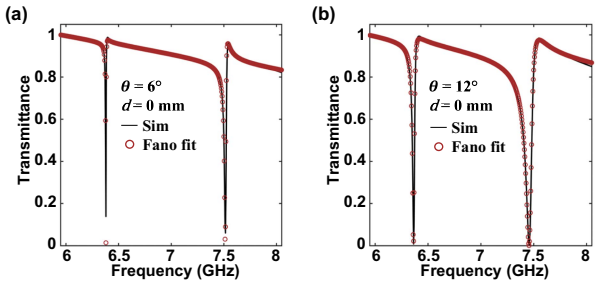

Fig. 7. Fano fitting of dual quasi-BICs at (a) $\theta = 6°$ and (b) $\theta = 12°$ with $d = 0$ mm.

APPENDIX B: THE EFFECT OF INTRINSIC LOSS OF MATERIALS ON MAXIMUM CHIRALITY

We keep all other parameters fixed in Fig. 5(d) and simulate the transmission of structures with different dielectric loss tangent $\tan(\delta)$ of the substrate, as illustrated in Figs. 8(a) and 8(b). Increasing $\tan(\delta)$ from 0.004 drastically elevates the $|t_L|^2$ minimum for quasi-BIC2 as the losses are critical for the CD. When $\tan(\delta)$ increases to 0.01, the $|t_L|^2$ minimum of two quasi-BICs is close to 0, indicating the appearance of maximum chirality. Increasing $\tan(\delta)$ far above 0.01 also negatively affects the CD value, especially for quasi-BIC1. Plot min $|t_L|^2$ values as a function of $\tan(\delta)$ [see the insets in Figs. 8(a) and 8(b)]. Therefore, intrinsic loss is also a necessary factor for maximum chirality.

We also discuss how to realize the maximum chirality at dual quasi-BICs frequencies under different dielectric loss tangent $\tan(\delta)$. The simulated transmissions of structures with

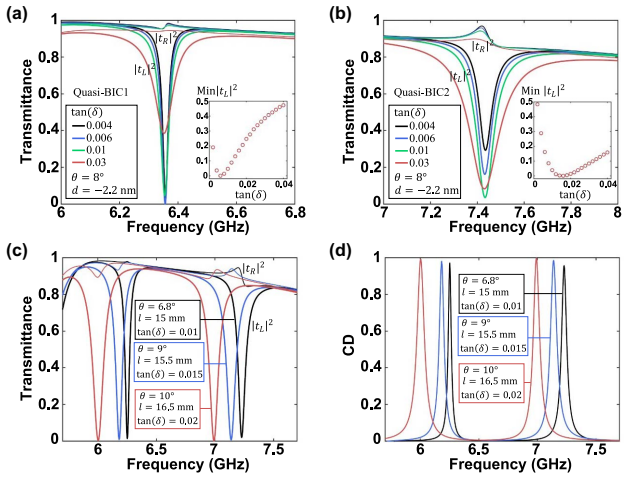

Fig. 8. RCP and LCP transmittance spectra of chiral metasurface with (a) quasi-BIC1 and (b) quasi-BIC2 uncoupled from RCP waves for different dielectric loss tangent tan(δ) of substrate. The insets indicate the simulated minimum transmittance with varying tan(δ). Spectra of (c) transmittance and (d) CD of metasurface hosting maximum chiral dual quasi-BICs with different tan(δ).

tan(δ) = 0.01, 0.015, and 0.02 are given in Fig. 8(c). With the increase of loss, longer metal wire l and larger incident angle θ can make the structure always match the maximum chirality, which has been proved by their CD spectra in Fig. 8(d). Strong tunability makes it possible to use different materials or in different bands to achieve maximum chirality.

APPENDIX C: THz METASURFACE SUPPORTING DUAL BICS WITH MAXIMAL CHIRALITY

We extend the chiral metasurface to THz wavelengths and prove that perfect dual-band circular dichroism can also be achieved. The material of the dielectric plate has been replaced with silicon dioxide from the original F4BM, ignoring intrinsic losses at the concerned wavelengths. Here, the dimensions of metal strips are $w = 25$ μm, $l = 100$ μm, and thickness $t = 0.035$ μm. The period of the unit cell p is 350 μm and the gap g is set to 26 μm. As we introduce relative vertical shift $d = -15.5$ μm and rotation angle $\theta = 8°$, the transmittance of LCP waves reaches 0.95 at two frequencies, while the transmittance of RCP waves is close to 0, as shown in Fig. 9(a).

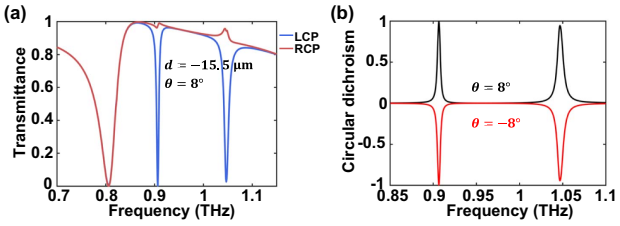

Fig. 9. (a) Transmittance spectra of the structure at $d = -15.5$ μm and $\theta = 8°$. The blue and red lines represent LCP and RCP waves, respectively. (b) CD value of the structure with $d = -15.5$ μm at opposite rotation angles.

The metasurface exhibits maximal chiroptical response driven by dual quasi-BICs. With opposite rotation angles θ, the near-perfect circular dichroism (|CD| > 0.95) also reverses, as shown in Fig. 9(b). Therefore, the basic principle and design method of our experiments in the microwave band can also be extended to other bands, such as the THz and infrared wavelengths.

Funding. National Key Research and Development Program of China (2021YFA1400602); National Natural Science Foundation of China (11974261, 62075213, 12104105, 12274325, 11874286, 61621001, 91850206).

Disclosures. The authors declare no conflicts of interest.

Data Availability. Data underlying the results presented in this paper are not publicly available at this time but may be obtained from the authors upon reasonable request.

REFERENCES

1. Y. Chen, J. Gao, and X. Yang, "Chiral metamaterials of plasmonic slanted nanoapertures with symmetry breaking," Nano Lett. **18**, 520–527 (2018).
2. M. Schüler, T. Pincelli, S. Dong, *et al.*, "Polarization-modulated angle-resolved photoemission spectroscopy: toward circular dichroism without circular photons and Bloch wave-function reconstruction," Phys. Rev. X. **12**, 011019 (2022).
3. Y. Chen, X. Yang, and J. Gao, "3D Janus plasmonic helical nanoapertures for polarization-encrypted data storage," Light Sci. Appl. **8**, 45 (2019).
4. E. Hendry, T. Carpy, J. Johnston, *et al.*, "Ultrasensitive detection and characterization of biomolecules using superchiral fields," Nat. Nanotechnol. **5**, 783–787 (2010).
5. M. Manoccio, M. Esposito, E. Primiceri, *et al.*, "Femtomolar biodetection by a compact core-shell 3D chiral metamaterial," Nano Lett. **21**, 6179–6187 (2021).
6. Y. Chen, X. Yang, and J. Gao, "Spin-controlled wavefront shaping with plasmonic chiral geometric metasurfaces," Light Sci. Appl. **7**, 84 (2018).
7. Q. Wang, E. Plum, Q. Yang, *et al.*, "Reflective chiral meta-holography: multiplexing holograms for circularly polarized waves," Light Sci. Appl. **7**, 25 (2018).
8. G. Zheng, H. Muhlenbernd, M. Kenney, *et al.*, "Metasurface holograms reaching 80% efficiency," Nat. Nanotechnol. **10**, 308–312 (2015).
9. C. Wu, H. Li, X. Yu, *et al.*, "Metallic helix array as a broadband wave plate," Phys. Rev. Lett. **107**, 177401 (2011).
10. S. Yoo and Q. H. Park, "Chiral light-matter interaction in optical resonators," Phys. Rev. Lett. **114**, 203003 (2015).
11. Z. Wang, F. Cheng, T. Winsor, *et al.*, "Optical chiral metamaterials: a review of the fundamentals, fabrication methods and applications," Nanotechnology **27**, 412001 (2016).
12. S. Yang, Z. Liu, S. Hu, *et al.*, "Spin-selective transmission in chiral folded metasurfaces," Nano Lett. **19**, 3432–3439 (2019).
13. Z. Li, W. Liu, H. Cheng, *et al.*, "Spin-selective full-dimensional manipulation of optical waves with chiral mirror," Adv. Mater. **32**, 1907983 (2020).
14. B. Semnani, J. Flannery, R. Al Maruf, *et al.*, "Spin-preserving chiral photonic crystal mirror," Light Sci. Appl. **9**, 23 (2020).
15. C. Wang, Z. Li, R. Pan, *et al.*, "Giant intrinsic chirality in curled metasurfaces," ACS Photonics **7**, 3415–3422 (2020).
16. M. Masyukov, A. Vozianova, A. Grebenchukov, *et al.*, "Optically tunable terahertz chiral metasurface based on multi-layered graphene," Sci. Rep. **10**, 3157 (2020).
17. Z. Wang, L. Jing, K. Yao, *et al.*, "Origami-based reconfigurable metamaterials for tunable chirality," Adv. Mater. **29**, 1700412 (2017).

18. V. A. Fedotov, P. L. Mladyonov, S. L. Prosvirnin, *et al.*, "Asymmetric propagation of electromagnetic waves through a planar chiral structure," Phys. Rev. Lett. **97**, 167401 (2006).
19. M. Qiu, L. Zhang, Z. Tang, *et al.*, "3D metaphotonic nanostructures with intrinsic chirality," Adv. Funct. Mater. **28**, 1803147 (2018).
20. W. Chen, Q. Yang, Y. Chen, *et al.*, "Extremize optical chiralities through polarization singularities," Phys. Rev. Lett. **126**, 253901 (2021).
21. Y. Hou, H. M. Leung, C. T. Chan, *et al.*, "Ultrabroadband optical superchirality in a 3D stacked-patch plasmonic metamaterial designed by two-step glancing angle deposition," Adv. Funct. Mater. **26**, 7807–7816 (2016).
22. M. Liu, D. A. Powell, R. Guo, *et al.*, "Polarization-induced chirality in metamaterials via optomechanical interaction," Adv. Opt. Mater. **5**, 1600760 (2016).
23. A. G. Mark, J. G. Gibbs, T. C. Lee, *et al.*, "Hybrid nanocolloids with programmed three-dimensional shape and material composition," Nat. Mater. **12**, 802–807 (2013).
24. P. Wang, R. Hu, X. Huang, *et al.*, "Terahertz chiral metamaterials enabled by textile manufacturing," Adv. Mater. **34**, 2110590 (2022).
25. Y. Zhao, M. A. Belkin, and A. Alù, "Twisted optical metamaterials for planarized ultrathin broadband circular polarizers," Nat. Commun. **3**, 870 (2012).
26. S. Yang, Z. Liu, H. Yang, *et al.*, "Intrinsic chirality and multispectral spin-selective transmission in folded eta-shaped metamaterials," Adv. Opt. Mater. **8**, 1901448 (2019).
27. J. Wu, H. Jiang, Z. Guo, *et al.*, "Giant optical chirality in dielectric metasurfaces induced by toroidal dipole resonances," Opt. Lett. **48**, 916–919 (2023).
28. J. Wu, X. Xu, X. Su, *et al.*, "Observation of giant extrinsic chirality empowered by quasi-bound states in the continuum," Phys. Rev. Appl. **16**, 064018 (2021).
29. W. Liu, B. Wang, Y. Zhang, *et al.*, "Circularly polarized states spawning from bound states in the continuum," Phys. Rev. Lett. **123**, 116104 (2019).
30. A. Y. Zhu, W. T. Chen, A. Zaidi, *et al.*, "Giant intrinsic chiro-optical activity in planar dielectric nanostructures," Light Sci. Appl. **7**, 17158 (2018).
31. C. W. Hsu, B. Zhen, A. D. Stone, *et al.*, "Bound states in the continuum," Nat. Rev. Mater. **1**, 16408 (2016).
32. P. Hu, C. Xie, Q. Song, *et al.*, "Bound states in the continuum based on the total internal reflection of Bloch waves," Natl. Sci. Rev. **10**, nwac043 (2023).
33. P. Hu, J. Wang, Q. Jiang, *et al.*, "Global phase diagram of bound states in the continuum," Optica **9**, 1353–1361 (2022).
34. A. F. Sadreev, "Interference traps waves in an open system: bound states in the continuum," Rep. Prog. Phys. **84**, 055901 (2021).
35. Z. Wang, Q. Xue, S. Zhao, *et al.*, "Study on the characteristics of a photonic crystal sensor with rectangular lattice based on bound states in the continuum," J. Phys. D **55**, 175106 (2022).
36. Y. Wang, Z. Han, Y. Du, *et al.*, "Ultrasensitive terahertz sensing with high-Q toroidal dipole resonance governed by bound states in the continuum in all-dielectric metasurface," Nanophotonics **10**, 1295–1307 (2021).
37. M. S. Hwang, H. C. Lee, K. H. Kim, *et al.*, "Ultralow-threshold laser using super-bound states in the continuum," Nat. Commun. **12**, 4135 (2021).
38. J. H. Yang, Z. T. Huang, D. N. Maksimov, *et al.*, "Low-threshold bound state in the continuum lasers in hybrid lattice resonance metasurfaces," Laser Photonics Rev. **15**, 2100118 (2021).
39. Q. Song, J. Hu, S. Dai, *et al.*, "Coexistence of a new type of bound state in the continuum and a lasing threshold mode induced by PT symmetry," Sci. Adv. **6**, 1160 (2020).
40. K. Koshelev, Y. Tang, K. Li, *et al.*, "Nonlinear metasurfaces governed by bound states in the continuum," ACS Photonics **6**, 1639–1644 (2019).
41. K. Koshelev, S. Kruk, E. Melik-Gaykazyan, *et al.*, "Subwavelength dielectric resonators for nonlinear nanophotonics," Science **367**, 288–292 (2020).
42. Z. Liu, Y. Xu, Y. Lin, *et al.*, "High-Q quasibound states in the continuum for nonlinear metasurfaces," Phys. Rev. Lett. **123**, 253901 (2019).
43. J. Li, J. Li, C. Zheng, *et al.*, "Spectral amplitude modulation and dynamic near-field displaying of all-silicon terahertz metasurfaces supporting bound states in the continuum," Appl. Phys. Lett. **119**, 241105 (2021).
44. J. Wang, L. Shi, and J. Zi, "Spin hall effect of light via momentum-space topological vortices around bound states in the continuum," Phys. Rev. Lett. **129**, 236101 (2022).
45. B. Wang, W. Liu, M. Zhao, *et al.*, "Generating optical vortex beams by momentum-space polarization vortices centred at bound states in the continuum," Nat. Photonics **14**, 623–628 (2020).
46. Y. Lin, T. Feng, S. Lan, *et al.*, "On-chip diffraction-free beam guiding beyond the light cone," Phys. Rev. Appl. **13**, 064032 (2020).
47. Z. Zhang, F. Qin, Y. Xu, *et al.*, "Negative refraction mediated by bound states in the continuum," Photonics Res. **9**, 1592–1597 (2021).
48. Z. Zhang, X. Yin, Z. Chen, *et al.*, "Observation of intensity flattened phase shifting enabled by unidirectional guided resonance," Nanophotonics **10**, 4467–4475 (2021).
49. X. Yin, J. Jin, M. Soljacic, *et al.*, "Observation of topologically enabled unidirectional guided resonances," Nature **580**, 467–471 (2020).
50. Y. Xie, Z. Zhang, Y. Lin, *et al.*, "Magnetic quasi-bound state in the continuum for wireless power transfer," Phys. Rev. Appl. **15**, 044024 (2021).
51. E. N. Bulgakov and A. F. Sadreev, "Bound states in the continuum in photonic waveguides inspired by defects," Phys. Rev. B **78**, 075105 (2008).
52. K. Koshelev, S. Lepeshov, M. Liu, *et al.*, "Asymmetric metasurfaces with high-Q resonances governed by bound states in the continuum," Phys. Rev. Lett. **121**, 193903 (2018).
53. F. Wu, J. Wu, Z. Guo, *et al.*, "Giant enhancement of the Goos-Hänchen shift assisted by quasibound states in the continuum," Phys. Rev. Appl. **12**, 014028 (2019).
54. F. Wu, D. Liu, and S. Xiao, "Bandwidth-tunable near-infrared perfect absorption of graphene in a compound grating waveguide structure supporting quasi-bound states in the continuum," Opt. Express **29**, 41975–41989 (2021).
55. A. Overvig, N. Yu, and A. Alù, "Chiral quasi-bound states in the continuum," Phys. Rev. Lett. **126**, 073001 (2021).
56. M. V. Gorkunov, A. A. Antonov, and Y. S. Kivshar, "Metasurfaces with maximum chirality empowered by bound states in the continuum," Phys. Rev. Lett. **125**, 093903 (2020).
57. M. V. Gorkunov, A. A. Antonov, V. R. Tuz, *et al.*, "Bound states in the continuum underpin near-lossless maximum chirality in dielectric metasurfaces," Adv. Opt. Mater. **9**, 2100797 (2021).
58. X. Zhang, Y. Liu, J. Han, *et al.*, "Chiral emission from resonant metasurfaces," Science **377**, 1215–1218 (2022).
59. K. H. Kim and J. R. Kim, "High-Q chiroptical resonances by quasi-bound states in the continuum in dielectric metasurfaces with simultaneously broken in-plane inversion and mirror symmetries," Adv. Opt. Mater. **9**, 2101162 (2021).
60. T. Shi, Z. L. Deng, G. Geng, *et al.*, "Planar chiral metasurfaces with maximal tunable chiroptical response driven by bound states in the continuum," Nat. Commun. **13**, 4111 (2022).
61. Q. S. Liu, M. H. Chao, W. J. Zhang, *et al.*, "Dual-band chiral nonlinear metasurface supported by quasibound states in the continuum," Ann. Phys. **534**, 2200263 (2022).
62. Y. Tang, Y. Liang, J. Yao, *et al.*, "Chiral bound states in the continuum in plasmonic metasurfaces," Laser Photonics Rev. **17**, 2200597 (2023).
63. H. Barkaoui, K. Du, Y. Chen, *et al.*, "Merged bound states in the continuum for giant superchiral field and chiral mode splitting," Phys. Rev. B **107**, 045305 (2023).
64. Y. Chen, H. Deng, X. Sha, *et al.*, "Observation of intrinsic chiral bound states in the continuum," Nature **613**, 474–478 (2023).
65. M. Gandolfi, A. Tognazzi, D. Rocco, *et al.*, "Near-unity third-harmonic circular dichroism driven by a quasibound state in the continuum in asymmetric silicon metasurfaces," Phys. Rev. A **104**, 023524 (2021).
66. H. J. Singh and A. Ghosh, "Large and tunable chiro-optical response with all dielectric helical nanomaterials," ACS Photonics **5**, 1977–1985 (2018).

67. W. T. Chen, K. Y. Yang, C. M. Wang, *et al.*, "High-efficiency broadband meta-hologram with polarization-controlled dual images," Nano Lett. **14**, 225–230 (2014).
68. F. Alpeggiani, N. Parappurath, E. Verhagen, *et al.*, "Quasinormal-mode expansion of the scattering matrix," Phys. Rev. X. **7**, 021035 (2017).
69. L. Cong and R. Singh, "Symmetry-protected dual bound states in the continuum in metamaterials," Adv. Opt. Mater. **7**, 1900383 (2019).
70. Y. Cai, Y. Huang, K. Zhu, *et al.*, "Symmetric metasurface with dual band polarization-independent high-*Q* resonances governed by symmetry-protected BIC," Opt. Lett. **46**, 4049–4052 (2021).
71. F. Wu, M. Luo, J. Wu, *et al.*, "Dual quasibound states in the continuum in compound grating waveguide structures for large positive and negative Goos-Hänchen shifts with perfect reflection," Phys. Rev. A **104**, 023518 (2021).
72. C. Zheng, J. Li, S. Wang, *et al.*, "Optically tunable all-silicon chiral metasurface in terahertz band," Appl. Phys. Lett. **118**, 051101 (2021).
73. D. Conteduca, I. Barth, G. Pitruzzello, *et al.*, "Dielectric nanohole array metasurface for high-resolution near-field sensing and imaging," Nat. Commun. **12**, 3293 (2021).